

Structure effects of exotic nuclei in the $A \approx 30$ mass region relevant for determining abundance patterns in explosive nucleosynthesis

R. Barman^{ⓧ,*}, S. Sarkar^{ⓧ,†} and R. Chatterjee^{ⓧ,‡}

Department of Physics, Indian Institute of Technology Roorkee, Roorkee 247 667, India

 (Received 3 May 2023; revised 2 July 2023; accepted 14 August 2023; published 24 August 2023)

Background: In the current understanding, the rapid neutron capture process in explosive scenarios primarily produces heavy elements. Though the precise astronomical sites are under consideration, it has been proposed that in explosive environments such as core-collapse supernovae, light and medium-mass neutron-rich nuclei play a role in the r process.

Purpose: Proper nuclear physics inputs for neutron-rich exotic nuclei are essential in determining the final abundances. The statistical Hauser-Feshbach model is not always reliable in the $A \approx 30$ mass region, especially for exotic nuclei. Therefore, inputs derived from models that account for the structure and reactions of exotic nuclei are necessary, which could affect the abundance patterns considerably.

Method: We perform an abundance calculation in the deformed $A \approx 30$ mass region for a network of neutron-rich Na, Mg, and Al isotopes adopting constant temperatures, 3.4 GK and 0.62 GK, and corresponding densities in a core-collapse supernova. We consider selected neutron capture and photodisintegration rates calculated with the finite-range distorted wave Born approximation (FRDWBA) method, including deformation effects, and shell model β decay rates, wherever possible, along with those from the JINA-REACLIB database. A comparison is also made with rates from the TALYS estimates.

Results: We observe a significant difference in abundances calculated by incorporating FRDWBA inputs along with the statistical inputs, compared with the results calculated using only the statistical model inputs, especially at 0.62 GK. The abundance patterns suggest that neutron capture reactions are not dominant at 3.4 GK, while at 0.62 GK, (n, γ) reactions mostly dominate, and more neutron-rich elements near the drip line are produced.

Conclusion: Incorporating the exotic structure of nuclei involved in reaction networks is important, even though the deformation effects may not have a major significance. At $T_9 = 0.62$, ^{35}Na and ^{36}Mg prefer to undergo β decay rather than capturing a neutron.

DOI: [10.1103/PhysRevC.108.025812](https://doi.org/10.1103/PhysRevC.108.025812)

I. INTRODUCTION

The rapid neutron capture process (r process) is thought to be responsible for the production of half of the heavier elements and some of the lighter elements in nature [1,2]. The astronomical sites for this process are still under active consideration. The possible scenarios where the r process may occur are some of the highly neutron-rich environments like neutron-star–neutron-star (NS-NS) mergers, neutron-star–black-hole (NS-BH) mergers, and core-collapse supernovae (CCSNe). The nucleosynthesis in the neutrino-driven wind (NDW) in CCSNe has been widely studied in the past decades [3,4]. The general scenario is that the seed nuclei in NDW are produced during the early stage of expansion when the α -capture reaction dominates. Later, when the temperature and density become relatively lower, the charged particle reactions slow down, and r -process nucleosynthesis

starts from the seed nuclei. But for a short dynamical expansion timescale, the production of seed nuclei is reduced which results in an enhancement in the neutron-to-seed ratio, as reported in [4]. In this work, the authors use the NDW model in a core-collapse supernova to study the r -process nucleosynthesis. At a short expansion timescale, the temperature and density fall rapidly, and the charged particle reactions do not produce enough seed nuclei. This results in enhancing the neutron-to-seed ratio, which may be sufficient to synthesize heavier r -process elements. Therefore, the neutron-to-seed ratio is an important parameter to determine the possibility of the occurrence of r -process nucleosynthesis in NDW associated with CCSNe. The high neutron-to-seed ratio can only be achieved by high entropy, fast expansion, and low electron fraction [5]. Recent studies indicate that NDW outflow may not exhibit these conditions and are only capable of producing weak r -process elements (up to $A \approx 125$) [6,7]. It is generally known that although many assumed conditions, like high entropies, are not found in many current simulations of NDW in CCSNe, they may be possible in other r -process scenarios (Ref. [8], for example). A very recent study shows that a secondary heating source within the NDW in a proton-neutron

*r_barman@ph.iitr.ac.in

†shahariar.ph@sric.iitr.ac.in

‡rchatterjee@ph.iitr.ac.in

star can change the hydrodynamic conditions which in turn, can help in the production of main r -process elements [9]. This suggests that one still cannot completely eliminate the possibility of NDW being one of the possible scenarios for r -process nucleosynthesis.

It was found in Ref. [4] that the inclusion of lighter neutron-rich nuclei in the full network can considerably change the final abundance patterns. Therefore, to understand the effect of these neutron-rich nuclei in producing the seed nuclei for the main r process, it is essential to accurately measure the (n, γ) reaction rates associated with these nuclei. However, direct experimental measurement is often difficult due to very low capture cross sections. Thus, one must rely on indirect methods with theoretical inputs to calculate the cross sections and reaction rates [10,11]. Various indirect methods, such as the asymptotic normalization constant (ANC) method [12], Trojan horse (TH) method [13,14], and Coulomb dissociation (CD) method [15,16] are some of the widely used methods that are used to calculate the reaction cross sections and rates of these nuclei. We are particularly interested in the CD method as, in this case, on choosing proper kinematic conditions, one can ensure a larger cross section that could be measurable [17].

The statistical Hauser-Feshbach model is used for the majority of the nuclear reaction calculations in astrophysical environments [18]. This model is particularly useful in situations when the level density around the peak of projectile energy in the contributing energy window is high enough to justify a statistical treatment. It is apparent in many studies that the statistical model estimates for most of the lighter neutron-rich nuclei with $A \approx 30$ differ significantly from the other theoretical calculations [19–21]. For example, in Ref. [21], the authors have calculated the reaction rates for $^{36}\text{Mg}(n, \gamma)^{37}\text{Mg}$ using the post-form finite-range distorted wave Born approximation (FRDWBA) theory. They have adopted the $^{36}\text{Mg}(0^+) \otimes 2p_{3/2}v$ configuration and a neutron separation energy, $S_n = 0.35$ MeV for the ground state of ^{37}Mg and compared the rates with the statistical Hauser-Feshbach model calculations. Another similar study [20] has been carried out for $^{33}\text{Na}(n, \gamma)^{34}\text{Na}$ adopting the $^{33}\text{Na}(3/2^+) \otimes 2p_{3/2}v$ configuration and $S_n = 0.17$ MeV. Both these reactions are very important in determining the r -process path of the Na and Mg isotopes in explosive nucleosynthesis, which can finally affect the final abundance pattern. A large discrepancy between these rates in both studies has been observed, which questions the reliability of this model for these neutron-rich nuclei. Therefore, a rigorous study of (n, γ) reactions of nuclei in this region is necessary to predict astrophysical abundances better.

In this work, we consider a small reaction network of neutron-rich isotopes of Na, Mg, and Al near the drip line and perform the abundance calculation at two different temperatures depicting two different nucleosynthesis scenarios in a core-collapse supernova. We incorporate the radiative neutron capture rates for the available nuclei calculated using CD method under the framework of FRDWBA theory that includes all the structure inputs of these exotic nuclei. A major advantage of FRDWBA theory is that it is a full-order quantum mechanical reaction theory and the breakup contributions

of the projectile cover the entire nonresonant continuum. Thus, one does not have to deal with the multipole strength distributions which is required in other theories [20,22,23]. The corresponding photodisintegration decay constants are also calculated. The goal is to observe how much difference it can make in the elemental abundances by including reaction inputs calculated with the FRDWBA approach, wherever possible in the network, along with the inputs from the statistical model, taken from the JINA-REACLIB database, when compared with the result calculated using only statistical estimates obtained from JINA-REACLIB database. The available experimental β -decay rates are taken from the JINA-REACLIB, others are calculated using the shell model. The β -decay rates are common for all sets of calculations done in this work. We also make a comparison of the result with inputs calculated from the TALYS code, to check the reliability of the statistical model in the region of interest.

In Sec. II, we present a formalism of our work. Brief descriptions using the CD method as an indirect approach to calculate radiative capture and photodisintegration rates and microscopic shell model calculations of β -decay rates are presented as inputs to abundance calculations. In Sec. III, we present our results and discussions, wherein the nuclear physics inputs and the subsequent abundance calculations are discussed. The summary and conclusions of our paper appear in Sec. IV.

II. FORMALISM

A. Radiative capture reactions

A fully quantum mechanical post-form FRDWBA theory with the inclusion of deformation effects [24,25] is used to calculate elastic breakup cross sections (like the relative energy spectrum) and subsequently the astrophysical reaction rates. The deformation is incorporated in this theory using the axially symmetric quadrupole-deformed potential.

Consider that a projectile a with substructures $b + c$ is made to break up in the Coulomb field of a heavy target t . The relative energy spectrum, $d\sigma/dE_{bc}$, corresponding to the process $a + t \rightarrow b + c + t$ is calculated using

$$\frac{d\sigma}{dE_{bc}} = \int d\Omega_{bc} d\Omega_{at} \left(\frac{2\pi}{\hbar v_{at}} \right) \frac{\mu_{at} \mu_{bc} p_{at} p_{bc}}{h^6} \times \sum_{\ell m} \frac{1}{2\ell + 1} |\beta_{\ell m}|^2, \quad (1)$$

where v_{at} is the velocity of the projectile with respect to the target, Ω_{bc} , Ω_{at} are the solid angles, μ_{bc} , μ_{at} , p_{bc} , and p_{at} are the reduced mass and momentum of $b - c$ and $a - t$ systems, respectively. $\beta_{\ell m}$ is the reduced transition amplitude [25] containing the ground state wave function, $\phi_a^{\ell m}(\mathbf{r})$, of the projectile a , with ℓ and m as the relative orbital angular momentum and its corresponding projection, respectively.

The quadrupole deformation parameter, β_2 enters through the short-ranged potential V_{bc} , the initial-state potential between the substructures b and c via [25,26]

$$V_{bc}(r) = V_0 f(r) - \beta_2 R V_0 \frac{df(r)}{dr} Y_2^0(\hat{r}). \quad (2)$$

Here, V_0 is the depth of the spherical Woods-Saxon potential and $f(r) = [1 + \exp(\frac{r-R}{a_0})]^{-1}$ with $R = r_0 A^{1/3}$, r_0 and a_0 being the radius and diffuseness parameters, respectively.

By evaluating the relative energy spectrum from Eq. (1), one can calculate the photodisintegration cross section using [15]

$$\frac{d\sigma}{dE_{bc}} = \frac{1}{E_\gamma} n_{\pi L} \sigma_{\pi L}^{\text{photo}}, \quad (3)$$

provided only a single multipolarity, π , with order L dominates. $n_{\pi L}$ is the virtual photon number which fully depends on the $a-t$ system. The γ energy, E_γ , is related to the relative energy, E_{bc} , by $E_\gamma = E_{bc} + S_n$, where S_n is the one-nucleon separation energy of the $(b+c)$ system. The photodisintegration decay constant is then calculated using the following relation [27]:

$$\lambda_\gamma = \frac{8\pi}{h^3 c^2} \int_0^\infty \frac{E_\gamma^2}{\exp(E_\gamma/kT) - 1} \sigma_{\pi L}^{\text{photo}} dE_\gamma. \quad (4)$$

The radiative capture cross section, $\sigma_{\pi L}^{\text{rad}}$ can be obtained from the photodisintegration cross section using the principle of detailed balance,

$$\sigma_{\pi L}^{\text{rad}} = \frac{2(2j_a + 1)}{(2j_b + 1)(2j_c + 1)} \frac{k_\gamma^2}{k^2} \sigma_{\pi L}^{\text{photo}}. \quad (5)$$

j_i 's are the spins of particle i , ($i = a, b, c$), and the wave number in the $(b+c)$ channel is given by $k = \sqrt{2\mu_{bc} E_{bc}/\hbar^2}$, while the photon wave number is $k_\gamma = E_\gamma/\hbar c$.

Subsequently, the radiative capture rate (\mathcal{R}) can be calculated by folding the capture cross section with the relative velocity v_{bc} of the $b+c$ system, corresponding to the relative energy, E_{bc} , and averaging over the Maxwell Boltzmann velocity distribution, where $\mathcal{R} = N_A \langle \sigma_{\pi L}^{\text{rad}} v_{bc} \rangle$.

B. β -decay constants from the nuclear shell model

The half-life is an important parameter that characterizes the β decay of a nucleus. The partial half-life is related to the transition probability $T^{i \rightarrow f}$ (also, equivalently the β -decay constant λ_β) between initial ($|i\rangle$) and final ($|f\rangle$) states as [28]

$$t_{1/2}^{i \rightarrow f} = \frac{\ln 2}{T^{i \rightarrow f}} = \frac{\kappa}{f_0 (B_F^{i \rightarrow f} + B_{GT}^{i \rightarrow f})}. \quad (6)$$

Here, $B_F^{i \rightarrow f}$ and $B_{GT}^{i \rightarrow f}$ are the Fermi and Gamow-Teller reduced transition probability between states $|i\rangle$ and $|f\rangle$, respectively, and the constant κ is defined as [28] $\kappa = 2\pi^3 \hbar^7 \ln 2 / m_e^5 c^4 G_F^2$, where m_e is the electron mass, c is the speed of light, and G_F is the Fermi coupling constant. In the calculation, we have used the experimentally measured value of $\kappa = 6147$ s [28]. The Fermi phase-space integral f_0 is calculated with the expression [28,29]

$$f_0 = \int_1^{E_0} F_0(Z_f, \varepsilon) p \varepsilon (E_0 - \varepsilon)^2 d\varepsilon, \quad (7)$$

where F_0 is the Fermi function, Z_f is the number of protons of the daughter nucleus, E_e is the total energy of the emitted electron. Other parameters are defined as [28] $\varepsilon = E_e/m_e c^2$, $E_0 = E_i - E_f/m_e c^2$, $p = \sqrt{\varepsilon^2 - 1}$, where

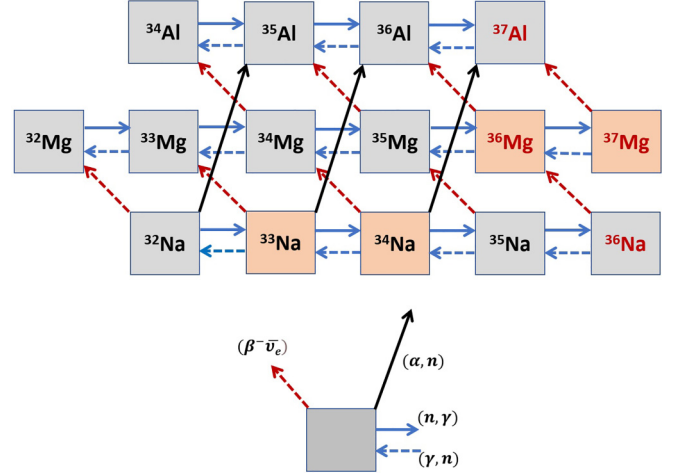


FIG. 1. Reaction network for neutron-rich Na, Mg, and Al isotopes.

E_i and E_f are the energy of the initial and final nuclear states, respectively. For β^- decay, we can also write $E_0 = (Q_{\beta^-} + m_e c^2)/m_e c^2$, where Q_{β^-} is the energy released in the decay.

The Fermi and Gamow-Teller reduced transition probabilities are defined as [28]

$$B_F^{i \rightarrow f} = \frac{g_V^2}{2J_i + 1} (|M_F^{i \rightarrow f}|^2), \quad B_{GT}^{i \rightarrow f} = \frac{g_A^2}{2J_i + 1} (|M_{GT}^{i \rightarrow f}|^2), \quad (8)$$

where $g_V = 1.0$ and $g_A = 1.27$ are the vector and bare axial-vector coupling constants of the weak interaction, respectively. The necessary Fermi $M_F^{i \rightarrow f}$ and Gamow-Teller $M_{GT}^{i \rightarrow f}$ nuclear matrix elements (NMEs) are calculated using the nuclear shell model [30]. In this approach, the many-body system is described by the Hamiltonian, which can be written in second quantization formalism in terms of single-particle energies ϵ_i , two-body matrix elements \hat{V}_{ijkl} , and creation (\hat{a}_i^\dagger) and annihilation (\hat{a}_i) operators as [30]

$$\hat{H} = \sum_i \epsilon_i \hat{a}_i^\dagger \hat{a}_i + \frac{1}{4} \sum_{ijkl} \hat{V}_{ijkl} \hat{a}_i^\dagger \hat{a}_j^\dagger \hat{a}_k \hat{a}_l. \quad (9)$$

The input parameters ϵ_i and \hat{V}_{ijkl} are used to construct the Hamiltonian of the many-body states, which are then diagonalized to obtain the eigenenergies and wave functions of the nuclei. These wave functions are subsequently used to calculate the one-body transition density (OBTD) which is the matrix element of neutron annihilation and proton creation operators between the initial and final nucleus. Finally, the $M_F^{i \rightarrow f}$ and $M_{GT}^{i \rightarrow f}$ are calculated using OBTD and single particle matrix elements of the decaying neutron and the final proton.

C. Nuclear network

The nuclear abundance is calculated considering a network for neutron-rich Na, Mg, and Al isotopes as shown in Fig. 1. For a nuclear species i , the abundance evolution is given by

the following differential equation [27]:

$$\frac{dN_i}{dt} = \left[\sum_{j,k} N_j N_k \langle \sigma v \rangle_{j,k \rightarrow i} + \sum_l \lambda_{\beta,l \rightarrow i} N_l + \sum_m \lambda_{\gamma,m \rightarrow i} N_m \right] - \left[\sum_n N_n N_i \langle \sigma v \rangle_{ni} + \sum_o \lambda_{\beta,i \rightarrow o} N_i + \sum_p \lambda_{\gamma,i \rightarrow p} N_i \right]. \quad (10)$$

Here, N_i is the number density of the species i , $\langle \sigma v \rangle$ is the reaction rate per particle pair for a particular reaction, and λ_{β} 's are the β -decay constants.¹ The terms in the first bracket of Eq. (10) represent all the processes producing the species i , whereas the terms in the second bracket represent the processes destroying the species i . In the first bracket, The first term represents the sum over all the reactions producing the species i via reactions between j and k ; the second term represents the sum over all β decays of nuclei l leading to i ; and the third term represents sum over all the photodisintegration reactions of nuclei m leading to nuclei i . Although λ_{γ} will be called the photodisintegration decay 'constant', unlike λ_{β} , it will vary with temperature.

Similar arguments are applied to the terms in the second bracket of Eq. (10). If a reaction between nonidentical particles ($j \neq k$) creates two species i , then the first term in the first bracket has to be multiplied by 2. If j and k are identical and produce one species of i , it must be divided by 2. Equation (10) holds for all other reactions, including identical particles. However, for three-particle reactions, one can refer to [31,32]. It is convenient to write Eq. (10) in terms of nuclear abundance, Y_i , instead of N_i , which is given by $Y_i = N_i / \rho N_A$, where ρ is the density of the stellar medium, and N_A is Avogadro's number.

Thus, Eq. (10) in terms of nuclear abundance Y_i would be

$$\frac{dY_i}{dt} = \left[\sum_{j,k} \rho N_A Y_j Y_k \langle \sigma v \rangle_{j,k \rightarrow i} + \sum_l \lambda_{\beta,l \rightarrow i} Y_l + \sum_m \lambda_{\gamma,m \rightarrow i} Y_m \right] - \left[\sum_n \rho N_A Y_n Y_i \langle \sigma v \rangle_{ni} + \sum_o \lambda_{\beta,i \rightarrow o} Y_i + \sum_p \lambda_{\gamma,i \rightarrow p} Y_i \right]. \quad (11)$$

In the next section, we will discuss a variety of nuclear physics inputs to Eq. (11), before proceeding to calculate the time evolution of abundance of all the nuclear species associated with the network that we have considered in Fig. 1.

III. RESULTS AND DISCUSSIONS

A. Nuclear physics inputs

The primary aim is to solve the coupled differential equations for the chosen network consisting of neutron-rich Na,

Mg, and Al isotopes at $T_9 = 3.4$ and $T_9 = 0.62$ adopting the conditions considered in [4] and subsequently display the abundance evolution with time. With this motivation, we focus on the nuclear physics inputs associated with the neutron-rich Na, Mg, and Al isotopes to investigate the changes in element-wise abundances.

Following Refs. [20,21], and Eqs. (5), (3), the $^{33}\text{Na}(n, \gamma)$ ^{34}Na and $^{36}\text{Mg}(n, \gamma)$ ^{37}Mg radiative capture, and $^{34}\text{Na}(\gamma, n)$ ^{33}Na and $^{37}\text{Mg}(\gamma, n)$ ^{36}Mg photodisintegration cross sections are computed with the FRDWBA theory, for $\beta_2 = 0.0$ (no deformation) and $\beta_2 = 0.5$ (with deformation). The (γ, n) photodisintegration constants [Eq. (4)] are also calculated by integrating from a lower limit, which is the one neutron separation energy (0.17 MeV for ^{34}Na and 0.35 MeV for ^{37}Mg) till the limit of convergence (≈ 6 MeV). The Maxwell-averaged radiative capture rates and the photodisintegration constants of the above reactions are shown in Fig. 2, as a function of temperature (in the units of 10^9 GK). The FRDWBA results, in light of the exotic nature of the nuclei involved, are shown for $\beta_2 = 0.0$ and $\beta_2 = 0.5$, with the black solid and green dashed line, respectively.

For the purpose of comparison, in Fig. 2, the other radiative capture rates and photodisintegration constants shown in red dotted and pink dash-dotted lines, and blue lines with crosses are obtained from the JINA-REACLIB database and the standard TALYS code (version 1.96), respectively. TALYS uses the statistical model to calculate Maxwell-averaged reaction rates at astrophysical temperatures treating the target nuclei in the ground as well as in excited states. In our calculations, we used the Gogny-Hartree-Fock-Bogoliubov model for level densities available in tabular format, the Brink-Axel Lorentzian model for the γ -ray strength function [33,34], and the Goriely HFB-Skyrme table for the theoretical mass model [35], if the experimental mass is not available. Incidentally, we did not see any perceptible change in the Q values for the $^{33}\text{Na}(n, \gamma)$ ^{34}Na or $^{36}\text{Mg}(n, \gamma)$ ^{37}Mg , 0.17 MeV and 0.24 MeV, respectively, while choosing the mass model options as HFB-Skyrme or the finite-range droplet model (FRDM). One may refer to [36] for more information regarding the TALYS inputs.

The Q values used in TALYS for the reactions shown in (a) and (b) of Fig. 2 are 0.17 MeV and 0.24 MeV, respectively, which are different from the Ref. [18] of JINA-REACLIB versions (1.208 MeV and -0.32 MeV, respectively). The large differences in Q values cause the rates to differ vastly from each other. In fact, we observe a completely different trend in reaction rates for the reaction $^{36}\text{Mg}(n, \gamma)$ ^{37}Mg shown in the pink dash-dotted line in panel (b) of Fig. 2, which arises due to the use of negative Q value in this reaction. However, the estimation of the same rates from Ref. [37], which is also a part of the JINA-REACLIB compilation for this reaction, shown by the red solid line, uses a Q value of 0.23 MeV, that is near to that used in TALYS. This generates a pattern that is similar to the TALYS result. Therefore, for the JINA-REACLIB compilation, we take the $^{36}\text{Mg}(n, \gamma)$ ^{37}Mg rate from Ref. [37], while the rest of the rates are from the more recent [18]. One notes that while in the former case [37], the mass model used is not apparent, in the latter [18], the FRDM is used.

¹While λ_{β} is constant, $\lambda_{\beta} N_i$, defined as the ' β -decay rate', will not be constant.

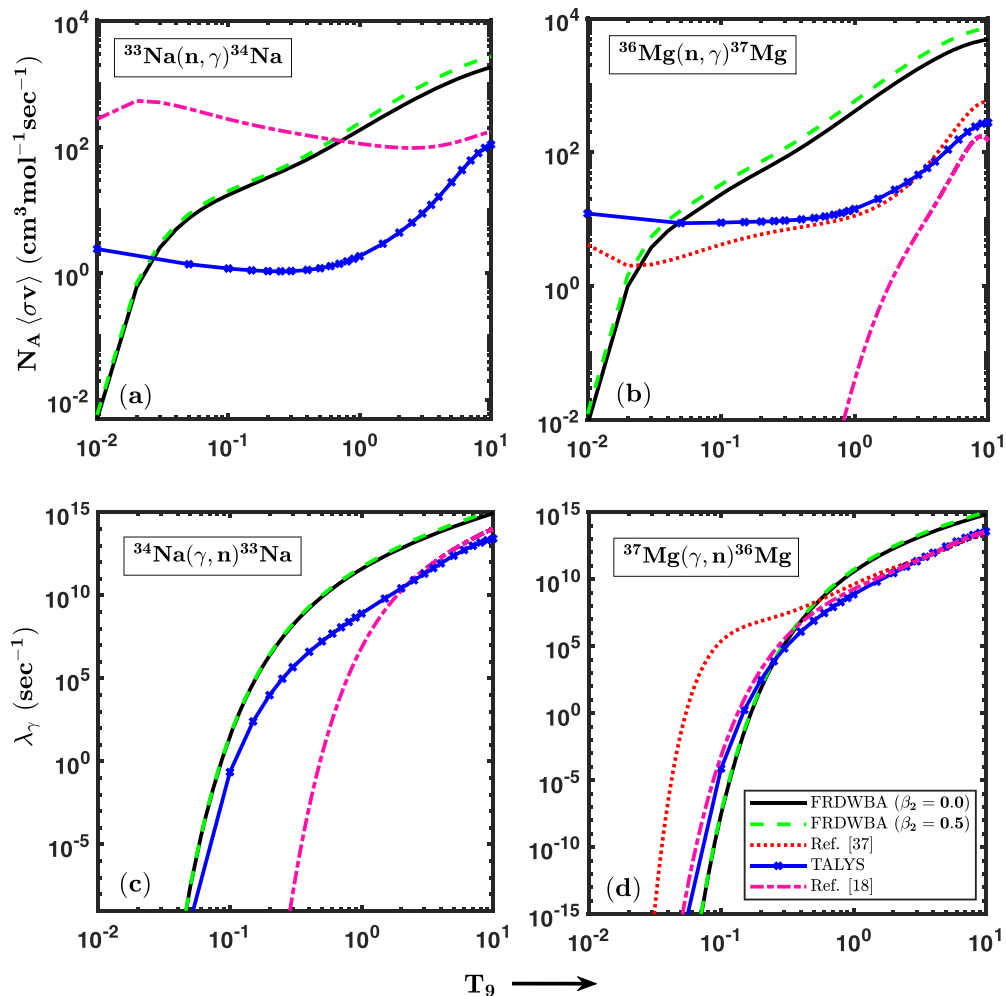


FIG. 2. The reaction rates for (a) $^{33}\text{Na}(n, \gamma)^{34}\text{Na}$, (b) $^{36}\text{Mg}(n, \gamma)^{37}\text{Mg}$, (c) $^{34}\text{Na}(\gamma, n)^{33}\text{Na}$, and (d) $^{37}\text{Mg}(\gamma, n)^{36}\text{Mg}$. The black solid lines represent the rates calculated using FRDWBA theory with no deformation ($\beta_2 = 0.0$), the green dashed lines represent FRDWBA rates including the deformation effect ($\beta_2 = 0.5$), the pink dash-dotted lines are the rates taken from Ref. [18], and the Ref. [37] in (b) and (d) are the rates taken from Ref. [37], as given in the JINA-REACLIB database. The blue lines with crosses are the rates calculated using TALYS.

It may be worth mentioning that the reaction rates from the FRDWBA calculations are not becoming zero at low temperatures but decreases as the temperature decreases, unlike statistical model calculations. Even though quantum tunneling may play a role in increased reaction rates at low temperatures, it is not unusual to observe the neutron capture rates decreasing at low temperatures in the classical picture, as the thermal energy of neutrons is very low at this temperature. In fact, as a function of energy, the neutron capture cross section extracted from the fully quantal Coulomb dissociation method was analyzed in Ref. [20], where it was shown that these cross sections are pretty sensitive to the neutron separation energies, and hence their structure. Depending on the kinematical conditions, one may even observe a reversal in the trends of these cross sections as a function of energy.

Similar features in neutron capture rates are also observed in Refs. [19] and [38], where the authors experimentally extract the photodisintegration and corresponding radiative neutron capture rates using the Coulomb dissociation method.

A comparison of reaction rates at two particular temperatures obtained from the FRDWBA model (for $\beta_2 = 0.0$ and $\beta_2 = 0.5$), the TALYS code, and JINA-REACLIB database is shown in Tables I and II. All the particle-induced (n, γ) and (α, n) rates considered in this work are shown in Table I, and the (γ, n) decay constants are shown in Table II. Furthermore, the provenance of the JINA-REACLIB data, i.e., Refs. [18] and [37], is shown by the superscript labels (a) and (b), respectively. We use these rates for the calculation of the abundance evolution of the nuclei at the temperatures of our interest.²

Table III shows the β -decay constants of the nuclei of our interest obtained from JINA-REACLIB, wherever available, and the shell model calculations for ^{36}Na and ^{37}Mg . We have used the shell model code KSHELL [39] for the evaluation of

²Since we use positive separation energies in our FRDWBA and TALYS calculations, we preferred the “older data” (positive Q value) from Ref. [37] for the reaction $^{36}\text{Mg}(n, \gamma)^{37}\text{Mg}$ in our calculations instead of the later ones (negative Q value) from Ref. [18], for the sake of consistency.

TABLE I. Comparison of the (n, γ) and (α, n) rates obtained from the JINA-REACLIB database and TALYS code along with those calculated from FRDWBA theory at $T_9 = 3.4$ and $T_9 = 0.62$.

Reaction	Reaction rates ($\text{cm}^3 \text{mol}^{-1} \text{s}^{-1}$) at $T_9 = 3.4$			Reaction rates ($\text{cm}^3 \text{mol}^{-1} \text{s}^{-1}$) at $T_9 = 0.62$		
	FRDWBA (β_2)	TALYS	REACLIB	FRDWBA (β_2)	TALYS	REACLIB
$^{32}\text{Na}(n, \gamma) ^{33}\text{Na}$	–	3.61×10^3	1.73×10^{2a}	–	4.91×10^3	3.63×10^{2a}
$^{33}\text{Na}(n, \gamma) ^{34}\text{Na}$	7.55×10^2 (0.0)	11.41	99.86 ^a	83.16 (0.0)	1.32	131.31 ^a
	9.80×10^2 (0.5)	–	–	1.03×10^2 (0.5)	–	–
$^{34}\text{Na}(n, \gamma) ^{35}\text{Na}$	–	1.65×10^3	1.44×10^{3a}	–	6.05×10^2	3.52×10^{3a}
$^{35}\text{Na}(n, \gamma) ^{36}\text{Na}$	–	11.32	0.204 ^a	–	0.15	2.14×10^{-10a}
$^{32}\text{Mg}(n, \gamma) ^{33}\text{Mg}$	–	7.33×10^3	2.92×10^{3a}	–	8.93×10^3	3.17×10^{3a}
$^{33}\text{Mg}(n, \gamma) ^{34}\text{Mg}$	–	1.23×10^4	5.92×10^{3a}	–	2.67×10^4	8.17×10^{3a}
$^{34}\text{Mg}(n, \gamma) ^{35}\text{Mg}$	–	1.80×10^2	1.22×10^{3b}	–	1.47×10^2	9.42×10^{2b}
$^{35}\text{Mg}(n, \gamma) ^{36}\text{Mg}$	–	8.47×10^3	2.36×10^{3a}	–	5.95×10^3	3.62×10^{3a}
$^{36}\text{Mg}(n, \gamma) ^{37}\text{Mg}$	1.99×10^3 (0.0)	55.81	60.34 ^b	2.04×10^2 (0.0)	11.19	8.94 ^b
	2.92×10^3 (0.5)	–	–	2.84×10^2 (0.5)	–	–
$^{34}\text{Al}(n, \gamma) ^{35}\text{Al}$	–	2.76×10^4	3.46×10^{4a}	–	4.38×10^4	9.35×10^{4a}
$^{35}\text{Al}(n, \gamma) ^{36}\text{Al}$	–	1.49×10^3	1.32×10^{3a}	–	1.45×10^3	2.11×10^{3a}
$^{36}\text{Al}(n, \gamma) ^{37}\text{Al}$	–	1.67×10^4	1.41×10^{4a}	–	2.92×10^4	2.80×10^{4a}
$^{32}\text{Na}(\alpha, n) ^{35}\text{Al}$	–	3.89×10^2	2.75×10^{4a}	–	1.91×10^{-8}	3.66×10^{-6a}
$^{33}\text{Na}(\alpha, n) ^{36}\text{Al}$	–	64.57	2.76×10^{4a}	–	2.24×10^{-9}	3.11×10^{-6a}
$^{34}\text{Na}(\alpha, n) ^{37}\text{Al}$	–	3.43×10^2	2.81×10^{4a}	–	4.28×10^{-8}	3.48×10^{-6a}

^aRef. [18]^bRef. [37]

^{36}Na and ^{37}Mg decay constants. First, the necessary many-body wave functions of the initial and final nucleus were obtained through shell model diagonalization. Then these states were used to calculate the OBTD that appears in the expression of Fermi and Gamow-Teller NMEs. The Fermi and Gamow-Teller NMEs are essential to evaluate the β -decay half-life and subsequently decay constant and rates. In this case, shell model Hamiltonian SDPF-MU [40] was used as

input. The SDPF-MU is an important shell model Hamiltonian for SDPF model space, which is a combined shell of SD and PF model space having the orbitals $1d_{5/2}$, $1d_{3/2}$, $2s_{1/2}$, $1f_{7/2}$, $1f_{5/2}$, $2p_{3/2}$, $2p_{1/2}$. The necessary nuclear states for the β decay of ^{36}Na and ^{37}Mg were calculated with up to two $\hbar\omega$ excitations. For the β decay of ^{36}Na , the calculated spin-parity was 2^- for the initial nucleus. For the final nucleus ^{36}Mg , we have considered all the allowed spin-parities for the Fermi

TABLE II. Comparison of the (γ, n) decay constants obtained from the JINA-REACLIB database and TALYS code along with those calculated from FRDWBA theory at $T_9 = 3.4$ and $T_9 = 0.62$.

Reaction	Decay constant (s^{-1}) at $T_9 = 3.4$			Decay constant (s^{-1}) at $T_9 = 0.62$		
	FRDWBA (β_2)	TALYS	REACLIB	FRDWBA (β_2)	TALYS	REACLIB
$^{32}\text{Na}(\gamma, n) ^{31}\text{Na}$	–	1.34×10^{11}	1.32×10^{11a}	–	6.72×10^{-2}	1.14×10^{-6a}
$^{33}\text{Na}(\gamma, n) ^{32}\text{Na}$	–	2.45×10^{10}	2.66×10^{11a}	–	1.11×10^{-10}	7.76×10^{5a}
$^{34}\text{Na}(\gamma, n) ^{33}\text{Na}$	4.22×10^{13} (0.0)	3.76×10^{11}	7.65×10^{11a}	3.11×10^{10} (0.0)	5.97×10^7	7.33×10^{2a}
	6.01×10^{13} (0.5)	–	–	3.87×10^{10} (0.5)	–	–
$^{35}\text{Na}(\gamma, n) ^{34}\text{Na}$	–	1.07×10^{11}	7.1×10^{10}	–	1.17×10^{-7}	4.65×10^{-3a}
$^{36}\text{Na}(\gamma, n) ^{35}\text{Na}$	–	3.47×10^{11}	6.27×10^{11a}	–	8.15×10^7	1.33×10^{9a}
$^{32}\text{Mg}(\gamma, n) ^{31}\text{Mg}$	–	4.33×10^7	2×10^{7a}	–	0.0	7.95×10^{-32a}
$^{33}\text{Mg}(\gamma, n) ^{32}\text{Mg}$	–	6.83×10^{10}	7.31×10^{10a}	–	5.37×10^{-6}	1.04×10^{-4a}
$^{34}\text{Mg}(\gamma, n) ^{33}\text{Mg}$	–	5.45×10^8	1.97×10^{8a}	–	0.0	1.80×10^{-25a}
$^{35}\text{Mg}(\gamma, n) ^{34}\text{Mg}$	–	3.47×10^{11}	3.40×10^{11a}	–	1.11×10^5	3.68×10^{8a}
$^{36}\text{Mg}(\gamma, n) ^{35}\text{Mg}$	–	1.3×10^{10}	4.62×10^{9a}	–	1.44×10^{-13}	1.75×10^{-17a}
$^{37}\text{Mg}(\gamma, n) ^{36}\text{Mg}$	1.96×10^{13} (0.0)	4.15×10^{11}	4.38×10^{11a}	3.11×10^{10} (0.0)	3.79×10^7	4.55×10^{8a}
	2.87×10^{13} (0.5)	–	–	1.14×10^9 (0.5)	–	–
$^{34}\text{Al}(\gamma, n) ^{33}\text{Al}$	–	4.65×10^{10}	1.38×10^{11a}	–	4.17×10^{-8}	1.29×10^{-6a}
$^{35}\text{Al}(\gamma, n) ^{34}\text{Al}$	–	8.08×10^7	5.31×10^{7a}	–	0.0	1.1×10^{-28a}
$^{36}\text{Al}(\gamma, n) ^{35}\text{Al}$	–	1.25×10^{11}	1.05×10^{11a}	–	2.69×10^{-3}	1.5×10^{-4a}
$^{37}\text{Al}(\gamma, n) ^{36}\text{Al}$	–	1.58×10^9	6.2×10^{8a}	–	1.47×10^{-20}	6.96×10^{-22a}

^aRef. [18]

TABLE III. The β -decay constants from the JINA-REACLIB database and shell model calculations.

Nuclei	^{32}Na	^{33}Na	^{34}Na	^{35}Na	^{36}Na	^{34}Mg	^{35}Mg	^{36}Mg	^{37}Mg
β -decay constant (s^{-1})	35.71 ^a	34.66 ^a	44.11 ^a	101.66 ^a	52.46 ^b	25.30 ^a	4.06 ^a	106.64 ^a	2.09 ^b

^aData from JINA-REACLIB (experimental).

^bShell model calculations.

and Gamow-Teller transition with excitation energy up to 15 MeV. For the decay of ^{37}Mg , the calculated initial spin-parity was $3/2^+$, and due to computational limitations, we were only able to include one $5/2^+$ state for the final nucleus, ^{37}Al . For other isotopes of Na and Mg, we considered the experimental β -decay constants from the JINA-REACLIB database.

Finally, we construct four sets of nuclear physics inputs based on the data in Tables I and II. The β -decay constants, considered in Table III, are common for all the sets.

- (i) set-I: Take available (n, γ) and (γ, n) rates from FRDWBA for $\beta_2 = 0.0$, and the other (n, γ) , (γ, n) and (α, n) rates from JINA-REACLIB.
- (ii) set-II: Take available (n, γ) and (γ, n) rates from FRDWBA for $\beta_2 = 0.5$, and the other (n, γ) , (γ, n) , and (α, n) rates from JINA-REACLIB.
- (iii) set-III: All the (n, γ) , (γ, n) , and (α, n) rates from JINA-REACLIB.
- (iv) set-IV: All the (n, γ) , (γ, n) and (α, n) rates from TALYS calculations.

Having fixed the nuclear physics inputs, let us now turn our attention to the network calculation and the study of the elemental abundances.

B. The abundance calculation

The astrophysical abundances have been calculated by solving the coupled differential equations [Eq. (11)] for the reaction network shown in Fig. 1. The hydrodynamic conditions for the chosen NDW model, given in [4], was originally adapted from [41]. The electron fraction, specific entropy, and dynamic expansion timescale were taken to be 0.42, 140 k_B /baryon and 5.1 ms, respectively. The initial abundances are adapted from Fig. 4(a), Fig. 5(a), and Fig. 7 of Ref. [4] and are shown in Table IV of the Appendix.

We discuss two cases with different temperature conditions during the expansion and evolve our network with time considering constant matter densities at that instant of time. This is definitely not the ideal case to neglect the hydrodynamic conditions, but, for simplicity, we can assume them to be constant since we note that the evolution of our network lasts for a very short period of time, as will be evident for the two cases considered below.

1. Case (a): $T_9 = 3.4$

$T_9 = 3.4$ corresponds to the time when α - capture dominates. Following Fig. 2 of Ref. [4], the matter density (ρ) corresponding to this temperature is 8.0×10^4 g/cm^3 , which is assumed to be constant throughout the network evolution. The inputs [4] for the neutron, α and proton abundances

(Y_n , Y_α and Y_p) are taken to be 0.19, 0.196, and 0.0296, respectively.

Figure 3 shows the variation of abundances of Na, Mg, and Al isotopes with time from the instant when the temperature reaches 3.4 GK. The black solid line and the green dashed line show the results with inputs from the considered FRDWBA rates for $\beta_2 = 0.0$ and $\beta_2 = 0.5$ in set-I and set-II, respectively. The red dotted and blue dash-dotted lines correspond to abundances calculated with all JINA-REACLIB (set-III) and TALYS (set-IV) inputs.

The evolution starts from a time when the neutron-rich Na and Mg isotopic abundances are very low compared to the Al abundances in the network. Compared with the β decay and neutron capture rates, the (α, n) charged particle rate dominates at this temperature and the isotopes ^{32}Na , ^{33}Na , and ^{34}Na are mostly used up in the production of the corresponding Al isotopes. The (n, γ) reactions are not very effective at this temperature. The evolution timescale at this temperature is also small, indicating that these elements burn out quickly at this temperature.

The abundance pattern for set-I and set-II data overlaps, which implies that there may not be any overt effect of deformation on the abundance pattern of nuclei for the network considered. We also notice a difference in abundances between set-I/set-II data and set-III data for some Na and Mg isotopes that are associated with the reactions for which the FRDWBA rates are included. There is also a quite significant difference in abundance calculated with set-IV inputs. Set-IV results indicate that Na isotopes should decay at a slower rate compared to the other sets at larger evolution times.

2. Case (b): $T_9 = 0.62$

$T_9 = 0.62$ corresponds to just before r -process freeze-out when the light neutron-rich nuclei contribute significantly to the production of seed nuclei, as reported in [4]. The matter density (ρ) corresponding to this temperature is 5.4×10^2 g/cm^3 . The neutron, α and proton abundances (Y_n , Y_α , and Y_p) are taken to be 0.017, 0.203, and 5.86×10^{-9} , respectively. All these inputs are adopted from Ref. [4]. As a matter of fact, the assumption of constant hydrodynamic conditions would be more appropriate for this scenario than Case (a), where the temperature and density may vary more.

Figure 4 shows the elemental abundance, at this temperature, for the neutron-rich Na-Mg-Al network considered with the four sets of nuclear physics inputs. The solid, dashed, and dotted lines represent the same sets, as mentioned in Case (a) and Fig. 3 earlier. The abundance pattern for set-I and set-II data overlaps, similar to the previous case, thereby reconfirming the insensitivity of the deformation parameter, even at this temperature. The difference in abundances

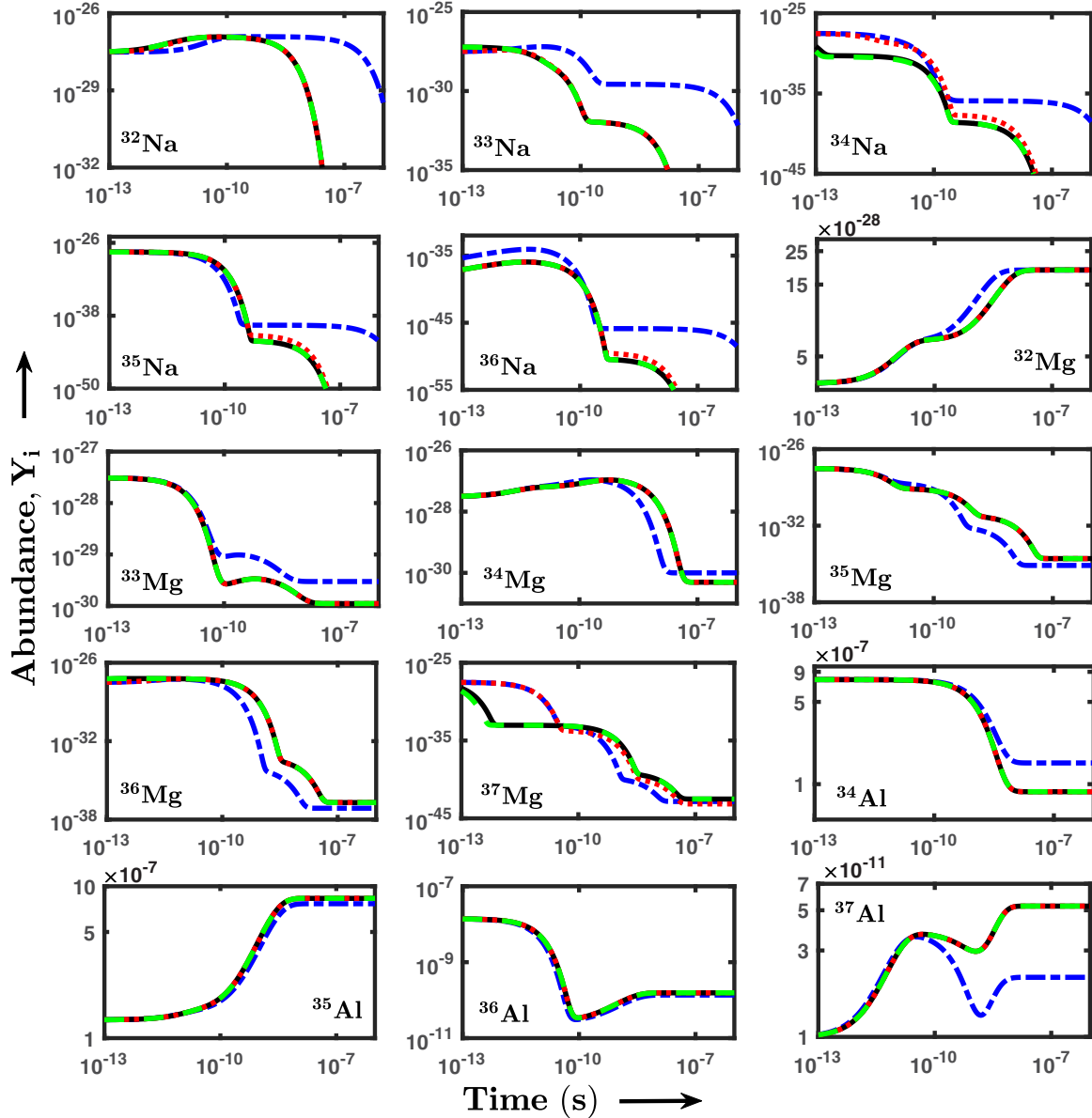


FIG. 3. Abundance (Y_i) evolution of neutron-rich Na, Mg, and Al isotopes at $T_0 = 3.4$ and $\rho = 8 \times 10^4$ g/cm³. The figure sublabels indicate the corresponding isotope. The black solid line and green dashed lines represent Y_i calculated using set-I and set-II data, the red dotted line represents Y_i calculated using the set-III data, and the blue dash-dotted line represents Y_i calculated using set-IV data. The description of different sets is given in the text.

between set-I/set-II data and set-III data is observed for some of the Na and Mg isotopes. The difference is more prominent compared to the previous case. The patterns for set-IV data also differ very much compared to the other sets. The (α, n) reactions do not contribute much to the abundance evolution at this temperature. In most cases, either the neutron capture and the photodisintegration reactions balance each other, or the neutron capture reactions dominate. During the freeze-out, at 0.62 GK, the neutron-rich Na and Mg isotopes are more abundant, and their evolutions are driven mainly by (n, γ) and β decays. The abundances drop after a certain time of their evolution (around 0.2 s) for all the nuclei, except ^{37}Al , whose abundance starts accumulating at a value around 5×10^{-5} .

We also plot the relevant production and decay rates of the nuclei ^{35}Na and ^{36}Mg in Fig. 5. We observe very small $^{35}\text{Na}(n, \gamma)^{36}\text{Na}$ and $^{36}\text{Na}(\gamma, n)^{35}\text{Na}$ rates for set-I, set-III, and set-IV data, that balances each other, as shown in panels (a), (b), and (c) of Fig. 5. Therefore, ^{35}Na must wait for its β decay before capturing a neutron which will cause less production of ^{36}Na , as apparent in Fig. 4. Although ^{36}Na is also produced from the β decay of ^{36}Mg , it does not add much to the production of ^{36}Na . Similarly, the $^{36}\text{Mg}(n, \gamma)^{37}\text{Mg}$ and $^{37}\text{Mg}(\gamma, n)^{36}\text{Mg}$ also attain equilibrium for all sets as shown in panels (d), (e), and (f) of Fig. 5, which indicates that ^{36}Mg will also wait for its β decay before further capturing a neutron. The constancy of the abundance patterns for ^{35}Na and ^{36}Mg , noted in Fig. 4, is also consistent with their β -decay

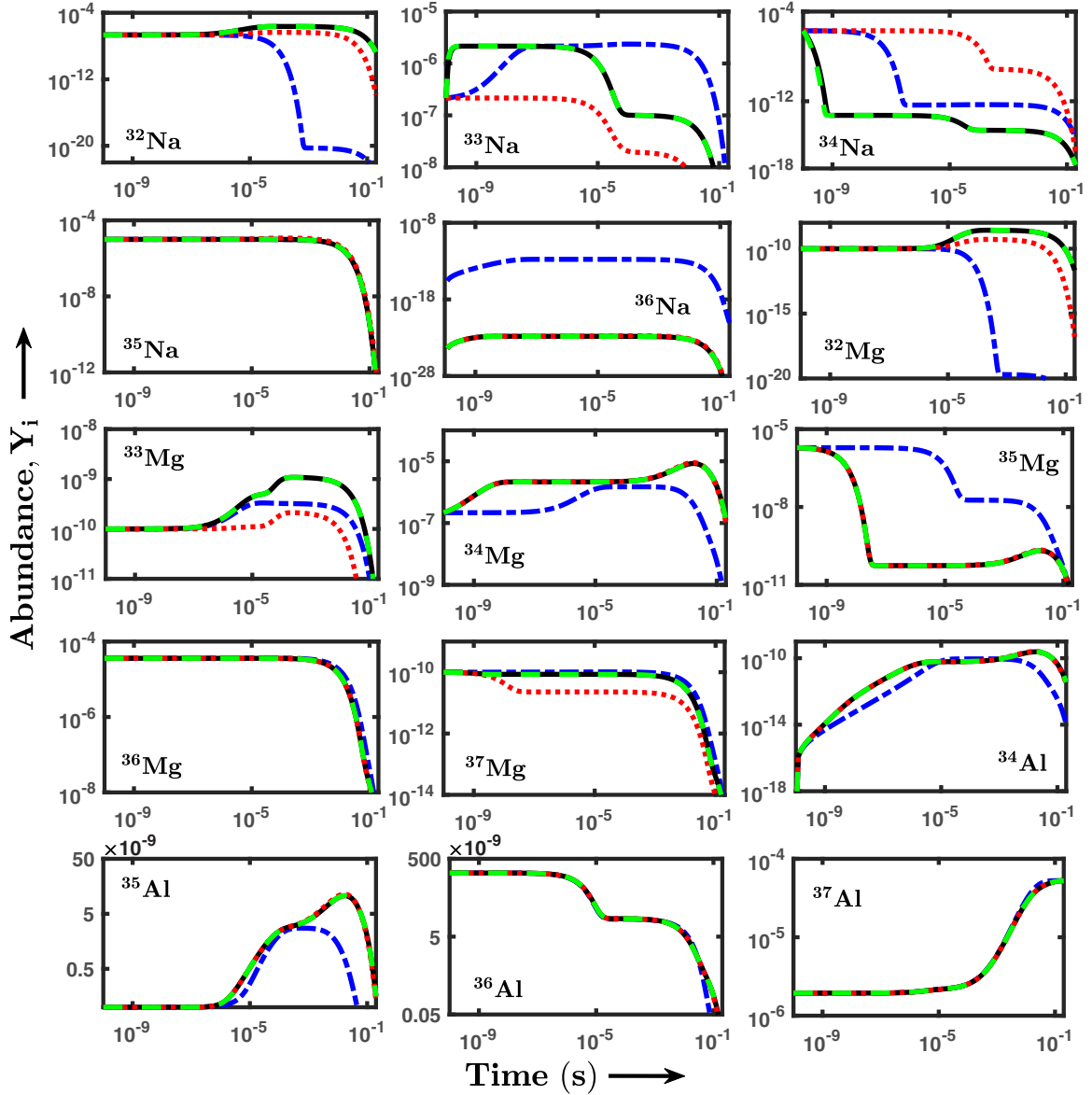


FIG. 4. Abundance (Y_i) evolution for Na-Mg-Al network at $T_9 = 0.62$ and $\rho = 5.4 \times 10^2 \text{ g/cm}^3$. The figure sublabels indicate the corresponding isotope. The legend has the same meaning as described in Fig. 3.

half-lives of 6.81 ms and 6.49 ms, respectively, estimated from Table III. This will hinder the abundance flow toward more neutron-rich elements, as also apparent in Fig. 4. The relatively low abundances for ^{36}Na and ^{37}Mg suggest that ^{35}Na and ^{36}Mg would most probably follow the β -decay path at this temperature, rather than capturing neutrons and pushing the abundance towards the drip-line.

We have checked the evolution of neutron and proton abundances in our network. At 3.4 GK, both the neutron and proton abundances are comparatively higher than the abundances of the nuclei in the network. Therefore, even though neutrons are being consumed, both Y_n and Y_p will change very slowly in magnitude. Similarly, the initial neutron abundance is also very high at 0.62 GK compared to the isotopic abundances of the elements, and therefore, the neutron fraction will be nearly constant over the network evolution timescale. However, the

proton abundance, initially very small at 0.62 GK, will sharply increase with time.

IV. SUMMARY AND CONCLUSIONS

It is now well known that light and medium mass neutron-rich nuclei play an important role in explosive nucleosynthesis. While it has been established in core-collapse supernovae, it ought to be valid for other astronomical sites supporting the r process, like neutron star mergers.

Exotic neutron-rich nuclei, especially those away from the valley of stability, have structures that are quite different from those of their stable counterparts. Some of them can have a halo structure and can also be deformed. Naturally, one would expect that incorporating the proper structure and reactions of

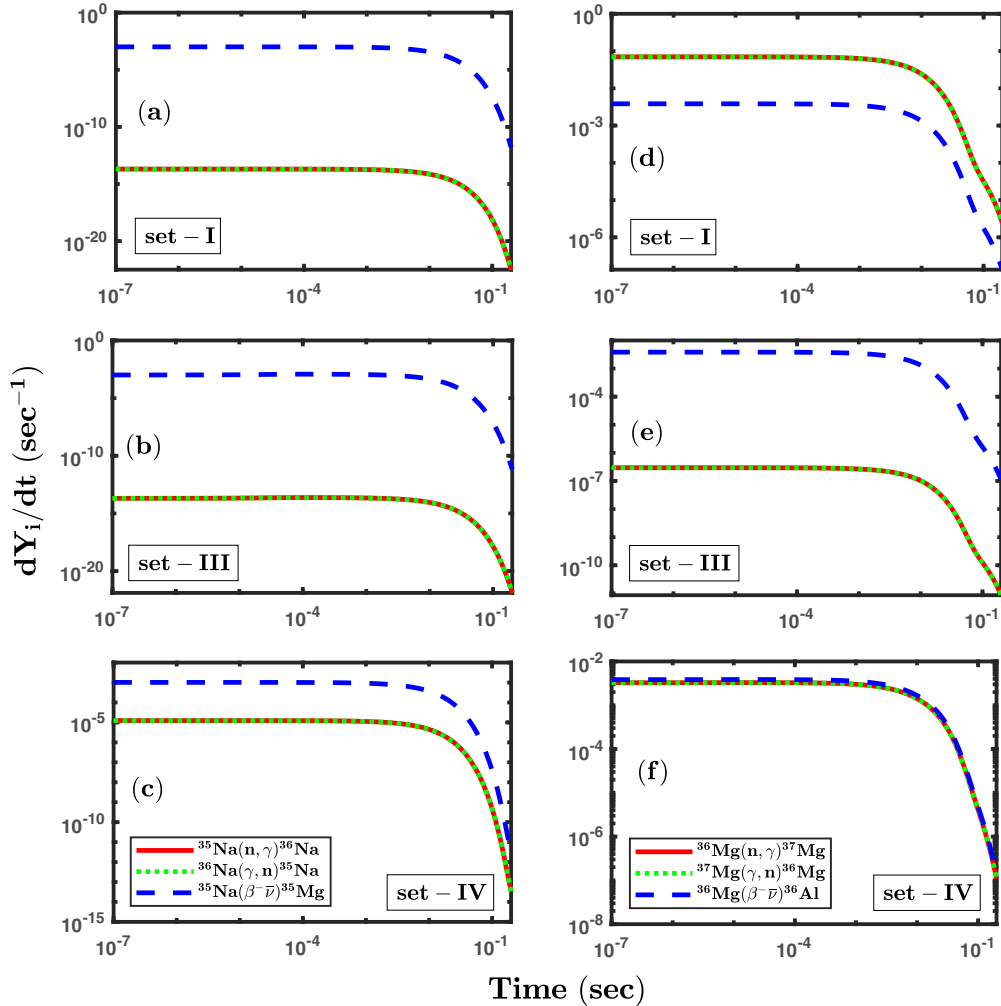


FIG. 5. The production and decay rate comparisons of ^{35}Na (left panel) and ^{36}Mg (right panel).

these nuclei would affect estimates of elemental abundances in various nucleosynthesis scenarios.

In most abundance calculations one is compelled to use statistical model estimates of nuclear reaction rates, especially in regions where there is scant data. However, the statistical treatment of the continua, especially for exotic nuclei may not always be justified.

In this work, we consider a network of neutron-rich Na-Mg-Al isotopes in the mass range of $A \approx 30$ and study their evolution with different sets of nuclear physics inputs. We have estimated neutron capture cross sections and photodisintegration constants for selected Na and Mg isotopes via the FRDWBA formalism, without and with deformation effects, and also estimated β -decay rates from the microscopic shell model. The rest of the rates are incorporated from the JINA-REACLIB database. We then calculate the element-wise abundance at two different temperatures portraying two different scenarios in a core-collapse supernova explosion with these inputs. In a sense, this reflects the effect of accounting for the exotic structures via the FRDWBA rates.

We have compared the results with those calculated using purely statistical model inputs from TALYS and the JINA-REACLIB database. We see vast differences in some of the

isotopic abundances at both temperatures. The theoretical models used in TALYS calculations differ from those used in rate calculations given in the JINA-REACLIB database. The observed discrepancies in pure statistical calculations could be due to the uncertainties associated with these theoretical models, different Q values of the reactions, etc. It is to be noted that for the case of ^{34}Na , the neutron separation energies were the same for FRDWBA and TALYS (0.17 MeV) while that extracted for JINA-REACLIB was larger (1.208 MeV). For ^{37}Mg it was similar for TALYS (0.24 MeV) and JINA-REACLIB (0.23 MeV), and was a bit higher for FRDWBA (0.35 MeV). Significant changes are also observed for FRDWBA-implemented (set-I/set-II) results in some of the isotopes at both temperatures. It is observed that the effect of deformation tends to increase the reaction rates by a small margin. However, no significant change is observed in the abundance patterns.

At 3.4 GK, the α -induced reactions dominate, and less production of neutron-rich isotopes via neutron capture reaction is observed. However, at $T_9 = 0.62$, mostly the neutron-induced reactions dominate thereby directing the abundance flow towards more neutron-rich nuclei. In our case, the mass fractions of the elements may not necessarily add up to 1,

TABLE IV. The initial abundances considered for our network as inputs to Eq. (11). They are adapted from Fig. 4(a), Fig. 5(a), and Fig. 7 of Ref. [4].

Nuclei	$(Y_i)_{t=0}$	
	$T_9 = 3.4$	$T_9 = 0.62$
^{32}Na	3.09×10^{-28}	2.16×10^{-7}
^{33}Na	3.09×10^{-28}	2.16×10^{-7}
^{34}Na	3.09×10^{-28}	1.94×10^{-6}
^{35}Na	3.09×10^{-28}	1×10^{-5}
^{36}Na	0.0	0.0
^{32}Mg	3.31×10^{-28}	1×10^{-10}
^{33}Mg	3.09×10^{-28}	1×10^{-10}
^{34}Mg	3.09×10^{-28}	2.16×10^{-7}
^{35}Mg	3.09×10^{-28}	1.93×10^{-6}
^{36}Mg	3.09×10^{-28}	3.6×10^{-5}
^{37}Mg	3.09×10^{-28}	1×10^{-10}
^{34}Al	7.73×10^{-7}	1×10^{-20}
^{35}Al	1.32×10^{-7}	1×10^{-10}
^{36}Al	1.39×10^{-8}	2.16×10^{-7}
^{37}Al	1×10^{-11}	1.94×10^{-6}
n	0.1856	0.0176
α	0.1958	0.2038
p	0.0295	5.86×10^{-9}

as we have considered only a limited number of nuclei in our network. However, the sum of the initial mass fractions considered at both temperatures comes out to be the same as the sum of the final mass fractions, which validates that our calculations are consistent.

Our calculations also suggest that at $T_9 = 0.62$, as the $(n, \gamma) \rightleftharpoons (\gamma, n)$ equilibrium is established, the nuclei ^{35}Na and ^{36}Mg would decay only via $^{35}\text{Na}(\beta^- \bar{\nu})^{35}\text{Mg}$ and

$^{36}\text{Mg}(\beta^- \bar{\nu})^{36}\text{Al}$ and the network will prefer to follow the path of the next isotopic chain rather than producing more neutron-rich elements in their respective chains.

Finally, let us remark that although we had taken a limited network, one must look into the full network calculations to describe the complete picture. In our calculations, we are more concerned about observing the sensitivity of the results by including the reaction inputs, which account for the exotic nature of the neutron-rich nuclei involved, by setting simple yet realistic conditions. It would be further interesting to perform a more systematic study of these effects in nucleosynthesis calculations for NS-NS and NS-BH mergers [42] with the full network.

ACKNOWLEDGMENTS

The authors thank the MoE, India, for the SPARC/2018-2019/P309/SL grant and doctoral research fellowship to R.B., SERB, DST, India for the SERB-National Post Doctoral Fellowship (PDF/2022/003729) to S.S., and the National Supercomputing Mission (NSM) for providing computing resources of ‘PARAM Ganga’ at IIT Roorkee (implemented by C-DAC and supported by MeitY and DST, India).

APPENDIX: INITIAL ABUNDANCE INPUTS IN SEC. III B

For a nucleus with atomic mass A_i , we can define a quantity called mass fraction which is given as $X_i = A_i Y_i$, representing the fraction of mass bound in species i . Based on the abundances given in Table IV, the sum of the initial mass fractions ($\sum_i A_i Y_i$), at $T_9 = 3.4$, is 0.998, while that at $T_9 = 0.62$, turns out to be 0.83. We have verified that the sum of the final mass fractions calculated at the end of our network evolution at both temperatures remains the same. This is not very surprising, as we have used a limited network.

- | | |
|---|---|
| <p>[1] J. J. Cowan, C. Sneden, J. E. Lawler, A. Aprahamian, M. Wiescher, K. Langanke, G. Martínez-Pinedo, and F.-K. Thielemann, <i>Rev. Mod. Phys.</i> 93, 015002 (2021).</p> <p>[2] T. Kajino, W. Aoki, A. Balantekin, R. Diehl, M. Famiano, and G. Mathews, <i>Prog. Part. Nucl. Phys.</i> 107, 109 (2019).</p> <p>[3] S. E. Woosley, J. R. Wilson, G. J. Mathews, R. D. Hoffman, and B. S. Meyer, <i>Astrophys. J.</i> 433, 229 (1994).</p> <p>[4] M. Terasawa, K. Sumiyoshi, T. Kajino, G. J. Mathews, and I. Tanihata, <i>Astrophys. J.</i> 562, 470 (2001).</p> <p>[5] A. Arcones and G. Martínez-Pinedo, <i>Phys. Rev. C</i> 83, 045809 (2011).</p> <p>[6] A. Arcones, H.-T. Janka, and L. Scheck, <i>Astron. Astrophys.</i> 467, 1227 (2007).</p> <p>[7] S. Shibagaki, T. Kajino, G. J. Mathews, S. Chiba, S. Nishimura, and G. Lorusso, <i>Astrophys. J.</i> 816, 79 (2016).</p> <p>[8] S. Wanajo and H.-T. Janka, <i>Astrophys. J.</i> 746, 180 (2012).</p> <p>[9] B. Nevins and L. F. Roberts, <i>Mon. Notices Royal Astron. Soc.</i> 520, 3986 (2023).</p> <p>[10] T. Aumann and C. A. Bertulani, <i>Prog. Part. Nucl. Phys.</i> 112, 103753 (2020).</p> <p>[11] F. Nunes, G. Potel, T. Poxon-Pearson, and J. Cizewski, <i>Annu. Rev. Nucl. Part. Sci.</i> 70, 147 (2020).</p> | <p>[12] H. M. Xu, C. A. Gagliardi, R. E. Tribble, A. M. Mukhamedzhanov, and N. K. Timofeyuk, <i>Phys. Rev. Lett.</i> 73, 2027 (1994).</p> <p>[13] S. Romano, C. Spitaleri, S. Cherubini, V. Crucillà, M. Gulino, M. L. Cognata, L. Lamia, R. G. Pizzone, S. M. R. Puglia, G. G. Rapisarda, M. L. Sergi, S. Tudisco, A. Tumino, R. E. Tribble, V. Z. Goldberg, A. M. Mukhamedzhanov, G. Tabacaru, L. Trache, V. Kroha, V. Burjan <i>et al.</i>, <i>J. Phys. G: Nucl. Part. Phys.</i> 35, 014008 (2008).</p> <p>[14] S. Typel, <i>Eur. Phys. J. A</i> 25, 665 (2005).</p> <p>[15] G. Baur, C. Bertulani, and H. Rebel, <i>Nucl. Phys. A</i> 458, 188 (1986).</p> <p>[16] R. E. Tribble, C. A. Bertulani, M. L. Cognata, A. M. Mukhamedzhanov, and C. Spitaleri, <i>Rep. Prog. Phys.</i> 77, 106901 (2014).</p> <p>[17] P. Banerjee, R. Chatterjee, and R. Shyam, <i>Phys. Rev. C</i> 78, 035804 (2008).</p> <p>[18] T. Rauscher and F.-K. Thielemann, <i>At. Data Nucl. Data Tables</i> 75, 1 (2000).</p> <p>[19] A. Bhattacharyya, U. Datta, A. Rahaman, S. Chakraborty, T. Aumann, S. Beceiro-Novo, K. Boretzky, C. Caesar, B. V. Carlson, W. N. Catford, M. Chartier, D. Cortina-Gil, P. Das, G. D. Angelis, P. D. Fernandez, H. Emling, H. Geissel, D.</p> |
|---|---|

- Gonzalez-Diaz, M. Heine, H. Johansson *et al.*, *Phys. Rev. C* **104**, 045801 (2021).
- [20] G. Singh, Shubhchintak, and R. Chatterjee, *Phys. Rev. C* **95**, 065806 (2017).
- [21] Shubhchintak, R. Chatterjee, and R. Shyam, *Phys. Rev. C* **96**, 025804 (2017).
- [22] S. Goriely, *Astron. Astrophys.* **325**, 414 (1997).
- [23] G. Baur, K. Hencken, and D. Trautmann, *Prog. Part. Nucl. Phys.* **51**, 487 (2003).
- [24] Shubhchintak, Neelam, R. Chatterjee, R. Shyam, and K. Tsushima, *Nucl. Phys. A* **939**, 101 (2015).
- [25] R. Chatterjee and R. Shyam, *Prog. Part. Nucl. Phys.* **103**, 67 (2018).
- [26] I. Hamamoto, *Phys. Rev. C* **69**, 041306(R) (2004).
- [27] C. Iliadis, *Nuclear Physics of Stars* (Wiley-VCH Verlag GmbH and Co. KGaA, Weinheim, 2007).
- [28] J. Suhonen, *From Nucleons to Nucleus: Concepts of Microscopic Nuclear Theory* (Springer, Berlin, 2007).
- [29] S. Yoshida, Y. Utsuno, N. Shimizu, and T. Otsuka, *Phys. Rev. C* **97**, 054321 (2018).
- [30] E. Caurier, G. Martínez-Pinedo, F. Nowacki, A. Poves, and A. P. Zuker, *Rev. Mod. Phys.* **77**, 427 (2005).
- [31] A. Chieffi, M. Limongi, and O. Straniero, *Astrophys. J.* **502**, 737 (1998).
- [32] W. R. Hix and B. S. Meyer, *Nucl. Phys. A* **777**, 188 (2006).
- [33] D. Brink, *Nucl. Phys.* **4**, 215 (1957).
- [34] P. Axel, *Phys. Rev.* **126**, 671 (1962).
- [35] S. Goriely, S. Hilaire, M. Girod, and S. Péru, *Eur. Phys. J. A* **52**, 202 (2016).
- [36] A. Koning and D. Rochman, *Nucl. Data Sheets* **113**, 2841 (2012).
- [37] F. K. Thielemann, M. Arnould, and J. W. Truran, in *Advances in Nuclear Astrophysics*, edited by E. Vangioni-Flam, J. Audouze, M. Casse, J.-P. Chieze, and J. Tran Thanh Van (Frontieres; Gif-sur-Yvette (France), 1986), pp. 525–540.
- [38] M. Röder, T. Adachi, Y. Aktyutina, J. Alcantara, S. Altstadt, H. Alvarez-Pol, N. Ashwood, L. Atar, T. Aumann, V. Avdeichikov, M. Barr, S. Beceiro, D. Bemmerer, J. Benlliure, C. Bertulani, K. Boretzky, M. J. G. Borge, G. Burgunder, M. Caamaño, C. Caesar *et al.* (R3B Collaboration), *Phys. Rev. C* **93**, 065807 (2016).
- [39] N. Shimizu, T. Mizusaki, Y. Utsuno, and Y. Tsunoda, *Comput. Phys. Commun.* **244**, 372 (2019).
- [40] Y. Utsuno, T. Otsuka, B. A. Brown, M. Honma, T. Mizusaki, and N. Shimizu, *Phys. Rev. C* **86**, 051301(R) (2012).
- [41] K. Sumiyoshi, H. Suzuki, K. Otsuki, M. Terasawa, and S. Yamada, *Publ. Astron. Soc. Japan* **52**, 601 (2000).
- [42] J. Lippuner and L. F. Roberts, *Astrophys. J.* **815**, 82 (2015).